RSC Advances

PAPER

View Article Online
View Journal | View Issue

Cite this: *RSC Adv.*, 2023, **13**, 20575

Ultrasensitive sensing performances of amphiphilic block copolymer induced gyrus-like In_2O_3 thick films to low-concentration acetone

Ling Li,*[a] Guiwen Wan,[a] Xinling Cui[a] and Yuwei Wang[b]

Received 8th May 2023
Accepted 24th June 2023

DOI: 10.1039/d3ra03063f

rsc.li/rsc-advances

In the present work, an inducible assembly of di-block polymer compounds approach was employed for the synthesis of mesoscopic gyrus-like In_2O_3 by using lab-made high-molecular-weight amphiphilic di-block copolymer poly(ethylene oxide)-*b*-polystyrene (PEO-*b*-PS) as a revulsive, with indium chloride as an indium source and THF/ethanol as the solvent. The obtained mesoscopic gyrus-like In_2O_3 indium oxide materials exhibit a large surface area and a highly crystalline In_2O_3 nanostructure framework, and the gyrus distance is about 40 nm, which can facilitate the diffusion and transport of acetone vapor molecules. By using this material as a chemoresistance sensor, the obtained gyrus-like indium oxides were used as sensing materials, showing an excellent performance to acetone at a low operating temperature (150 °C) due to their high porosity and unique crystalline framework. The limit of detection of the thick-film sensor based on indium oxides is appropriate for diabetes exhaled breath acetone concentration detection. Moreover, the thick-film sensor shows a very fast response–recovery dynamics upon contacting acetone vapor due to its abundant open folds mesoscopic structure, and also to the large surface area of the nanocrystalline gyrus-like In_2O_3.

1. Introduction

Acetone is widely used in many fields of industrial production because of its chemical activity, which is considered as one of the important raw materials, solvents and combustible gases.[1,2] In addition, in human breath there are hundreds of species of volatile organics which are exhaled from the blood through breath in the lungs. Expiratory analysis has attracted much attention among potential diagnostic techniques because of its noninvasive and real-time diagnostic advantages. In the breath of healthy people, the average concentration is below 0.9 ppm, while in diabetics, it is usually above 1.8 ppm.[3–8] Therefore, acetone can be used as a good biomarker for detecting diabetes in breath analysis. In order to detect diabetes mellitus by using an exhaled gas sensor, it is required that gas sensing material should show a large response under the condition that the concentration of acetone is very low, especially in a humid environment and under a complex background gas with different oxygen concentrations.

Many binary oxides or their composites (such as SnO_2,[9–12] ZnO,[13–16] WO_3,[17–19] NiO,[20,21] Fe_2O_3,[22,23] Co_3O_4,[24] TiO_2,[25–28] CuO–ZnO,[29] and ZnO–In_2O_3 (ref. 30)) have been found to be useful as acetone sensors. In recent years, indium oxide-based gas sensing materials have attracted extensive attention in the detection of low-concentration acetone gas. Gas sensors based on indium oxide and its derivatives react well to acetone. Different oxide morphologies (such as thick film, thin film, nanoparticles, bulk) have a great influence on the gas sensing performance of gas sensors.[31–40] In addition, the response to various reducing gases can be improved by compounding certain materials in inorganic oxides and perovskite oxides, such as $LaFeO_3$, $SmFeO_3$, $NdFeO_3$, $Yb_2Fe_3O_7$, $CdSnO_3$, $La_{1-x}Pb_xFeO_3$ *etc.*[41–54] In addition, lots of efforts have been made in order to synthesize highly effective indium oxide to improve the performance of In_2O_3-based nanomaterials and devices with different morphologies and sizes to promote the guest gas molecules' diffusion. Meanwhile, increasing the surface area provides abundant exposed active sites for kinds of interface adsorption, electron transport, reactions and host–guest interactions.

Different forms of In_2O_3 nanostructures which have various forms and morphologies, such as nanosheets, nanowires, nanospheres, nanotubes, nanoflowers, and layered nanostructures, are prepared by hydrothermal and solvothermal preparation of $In(OH)_3$ or InOOH,[55–59] followed by calcination treatment. Methods of electrospinning, chemical vapor deposition, polymer templating, laser ablation, self-templating *etc.* can also be used to prepare large specific surface area In_2O_3 nanocrystalline materials.[60–70] Acetone sensing properties for various semiconductor sensors are shown in Table 1. However, the above methods often result in ill-defined convoluted

---

[a] *School of Materials Science and Engineering, Shandong Jianzhu University, Jinan 250100, China. E-mail: 13866@sdjzu.edu.cn*

[b] *Technology and Information Technology Department, China Railway Jinan Group Co. Ltd, Jinan 250001, China*

Table 1 Acetone sensing properties for various semiconductor sensors

Author	Materials	T (°C)	Acetone concentration (ppm)	Response	Reference
Suparat Singkammo *et al.*	Ni-doped SnO_2 composite film	350	200	54.2	3
S. B. Patil *et al.*	Co-doped SnO_2 thin films	270	60	32	9
M. Punginsang *et al.*	Co-doped SnO_2 thin films	250	20	36.9	10
R. K. Mishra *et al.*	SnO_2 nanoparticles	250	10	42	11
W. X. Jin *et al.*	SnO_2 nanoflowers	260	25	40	12
S. Wei *et al.*	ZnO hollow nanofibers	220	1	7.1	13
D. An *et al.*	ZnO nanomaterials	220	100	6.0	14
C. Peng *et al.*	ZnO hollow nanofibers	300	100	18.6	15
N. H. Al-Hardan *et al.*	Cr-doped ZnO films	400	500	90	16
D. Chen *et al.*	WO_3 nanoparticle	300	2	2	17
S. Kim *et al.*	WO_3 with both Pd and Au	300	200	152.4	19
L. Wang *et al.*	Au-doped NiO hybrid structure	240	20	7.6	20
C. Wang *et al.*	W-doped NiO films	250	100	198.1	21
Hao Shan *et al.*	La-doped α-Fe_2O_3 nanomaterials	240	50	26	22
Chang Su *et al.*	Sm-doped α-Fe_2O_3 nanomaterials	240	0.5	2.3	23
Z. Zhang *et al.*	Co_3O_4 nanosheets	150	10	1.7	24
M. Epifani *et al.*	TiO_2 nanocrystals	400	100	1.2	26
B. Bhowmik *et al.*	TiO_2 nanotubes	27	10	1.136	27
H. Bian *et al.*	TiO_2 nanorods	500	10	9	28
C. Wang *et al.*	CuO–ZnO nanoparticles	340	10	3.7	29
X. Chi *et al.*	ZnO–In_2O_3 composite nanotubes	280	60	43.2	30
Z. L. Wu *et al.*	$NdFeO_3$	120	50	300	47
T. Chen *et al.*	$SmFeO_3$	250	380	2.6	48
X. Liu *et al.*	$SmFe_{0.9}Mg_{0.1}O_3$	260	300	353	49
X. Liu *et al.*	$LaFeO_3$	400	80	204	50
L. Zhang *et al.*	$La_{0.68}Pb_{0.32}FeO_3$	200	50	7	51
S. Zhang *et al.*	In_2O_3 nanospheres	350	10	53.08	65
S. Park *et al.*	In_2O_3–TiO_2	250	1	10	66
F. Chen *et al.*	In_2O_3	250	50	12	67
W. Liu *et al.*	Pt–In_2O_3	180	10	15.1	68
Y. Che *et al.*	In_2O_3	200	100	37.9	69
Z. Song *et al.*	Pt–In_2O_3	300	10	113	70

structures and uncontrolled morphology and porosity. It was found that these materials have remarkable electrochemical and gas sensing properties due to their large specific surface area and interconnected mesoscopic structure. In addition, the induction synthesis method for the inducer is more suitable and flexible for the production of high-performance sensing materials with large surface area. However, due to the difficulty in controlling the self-assembly and crystallization process of organic templates and inorganic precursors, there are few studies on the synthesis of sensing materials with high sensing efficiency and large surface area by flexible soft template-induced synthesis.

In this work, mesoscopic gyrus-like indium oxide with two-dimensional porous nanowalls synthesized from a high-molecular-weight di-block copolymer (PEO-*b*-PS) induced the In_2O_3 simple. Due to the support from the rigidity of the PS segments during the process of synthesis, the mesoscopic structure can be well obtained after ordered annealing in the air. This results in the mesoscopic gyrus-like nano-In_2O_3 with large specific area structure. Mesoscopic gyrus-like In_2O_3 materials have high porosity and unique crystal structures, and have excellent sensing properties to low-concentration acetone, such as fast response and recovery time, detection limit of sub-ppb and good selectivity in different gases. This excellent performance makes possible the use of intelligent gas sensors based on this In_2O_3 structure, which can be used in many fields, especially the non-invasive diagnosis of diabetes.

2. Materials and methods

2.1. Synthesis of mesoscopic grooved indium oxide

The laboratory-prepared amphiphilic block copolymer PEO112-*b*-PS165 synthesized according to an existing related research report[64] was dissolved in 4.5 mL THF, and then a solution can be obtained. And then, 0.3 g of indium trichloride was dissolved in 3 mL ethanol. The two solutions were then mixed and stirred for half an hour to form a transparent and colorless solution. Then the solution was poured into a watch glass, the solvent was placed at room temperature for 2 hours (ambient humidity was controlled to <40% in order to prevent the $InCl_3$ hydrolysis reaction with the water in the air), and then heated continuously at 60 °C for 5 hours and at 100 °C for 12 hours. Then the translucent film in a glass container was calcined in a muffle furnace at 400 °C with appropriate amount of CaO_2 for 30 minutes at a rate of 4 °C min^{-1}. Finally, the rolled film was ground into a yellow uniform powder.

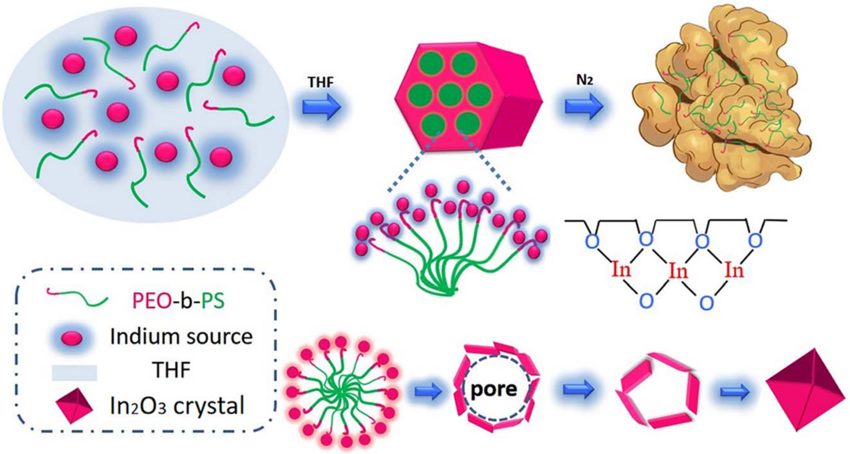

Fig. 1 Illustration of the synthesis of mesoscopic gyrus-like In_2O_3.

2.2. Synthesis of mesoscopic grooved In_2O_3 nanocrystals

Fig. 1 illustrates the synthesis of indium oxide, firstly with the mixed solution including PEO112-*b*-PS165 di-block copolymer, ethanol, $InCl_3$, and THF. With the solvent (mainly THF) at an ambient temperature of about 25 °C, the dissolved PEO-*b*-PS copolymer then gradually aggregated into columnar micelles with the PS segment as the gyrus because of the hydrophilic and hydrophobic end-to-end arrangement. Simultaneously part of the hydrolyzed hydrophilic inorganic indium interacted with the end of PEO by weak coordination bonds and hydrogen bonds. With the THF in the solution evaporating, a uniform and transparent rolled film formation was observed in the watch glass. Finally, the organic–inorganic hybrid membrane attached on the watch plate was prepared at 400 °C for 30 min. Calcium oxide was used to promote the decomposition of PEO-*b*-PS organics, the mesostructure being protected by the rapid release of oxygen. A series of mesoscopic gyrus-like In_2O_3-x-y-z nanocrystalline materials were synthesized, where x, y, z are related to the proportion by weight of PEO-*b*-PS polymer and $InCl_3$, the annealing temperature and the time, respectively. Fig. 1 illustrates the induced assembly process for the mesoscopic gyrus-like In_2O_3 starting from the solution with the mixture containing PEO-*b*-PS di-block copolymer *etc.*

A certain amount of indium oxide product synthesized by induction was mixed with an appropriate amount of deionized water, and then the mixture was loaded on an Al_2O_3 ceramic tube with two electrodes at one end in the form of a thick film. The ceramic tube was approximately 10 mm long, with an outer diameter of approximately 8 mm and an inner diameter of approximately 5 mm (Fig. 2). To improve the repeatability and stability, the gas sensor should be calcined at 200 °C for 3 h. The gas sensing properties of the nanocrystalline material were measured in the temperature range of 100–200 °C. The resistance of the sensor was measured in the air and guest gas (test), dry air being used as the carrier gas. The sensitivity of the thick-film sensor to the test gas is defined as $S = R_a/R_g$, where R_a is the resistance in air and R_g is the resistance in the test gas.

3. Results and discussion

3.1. The X-ray diffraction (XRD) and the scanning electron microscope (SEM)

Wide angle X-ray diffraction (XRD) measurements showed that the In_2O_3-400-0.5 sample obtained after calcination of the prepared PEO-*b*-PS/In_2O_3 showed excellent resolved diffraction peaks in the 20–80° range (Fig. 3), consistent with the crystal-centered cubic phase of In_2O_3 (JCPDS no. 06-0416), which has no other diffraction peaks. Also, no other crystalline impurities were detected in the XRD pattern, indicating that In_2O_3 was purely crystalline. According to scanning electron microscopy (SEM), mesoscopic outer In_2O_3 indium oxide materials are observed, with an orderly walnut shape of the outer structure. With the change of calcination temperature, the nano structure of the samples shaped to be layer and block through carefully

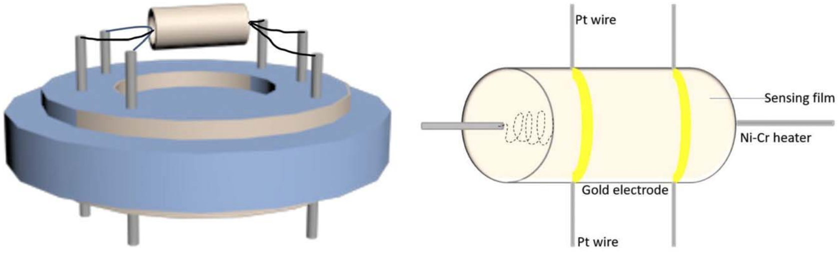

Fig. 2 Schematic of the thick-film sensor.

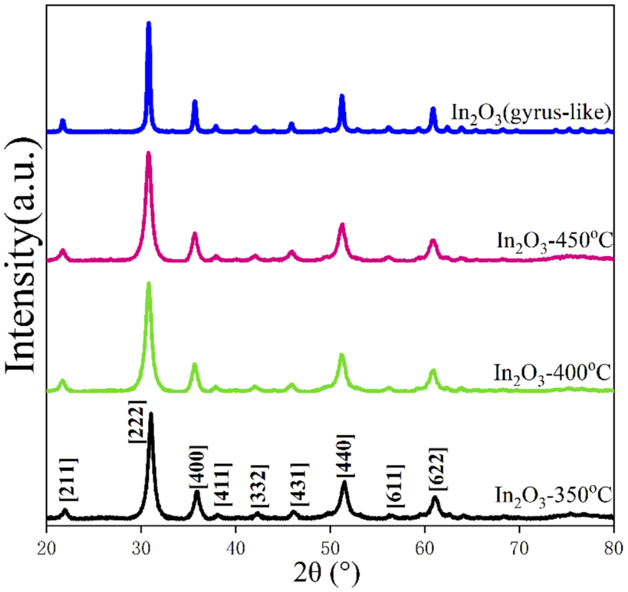

Fig. 3 The X-ray diffraction patterns of In_2O_3 annealed at different temperatures.

observation. According to the SEM images, the outer gap diameter is estimated at about 40 nm (Fig. 4).

In order to investigate the crystallization behavior of In_2O_3 gyrus walls during the annealing process, non-PEO-*b*-PS-In_2O_3 hybrid nanocrystalline material was prepared and calcined at 400 °C and 450 °C for 0.5 h in air with a low-humidity environment. The results show that increasing of the annealing temperature at 400 °C can make In_2O_3 nanograins (without PEO-*b*-PS) grow large into nanosheets which have larger size about (400 nm × 300 nm), larger thickness (20–25 nm) and higher crystallinity (Fig. 5a). During this heating-up annealing process, the two-dimensional lamella layer morphology remains intact. By comparison, with the calcination temperature increasing from 400 °C to 450 °C, the nano-lamella layer In_2O_3 rapidly disappeared and discrete rhomboid octahedral particles with diameters of 500 nm were formed (Fig. 5b). This means that a calcination temperature as high as 450 °C can cause a significant change in the structure and morphology of gyrus indium oxide, and this is a typical thermodynamic transformation reaction process. And a further extension of the annealing time to 30 min at 450 °C resulted in the formation of In_2O_3 discrete particles with the shape of unique octahedra, which also is a typical

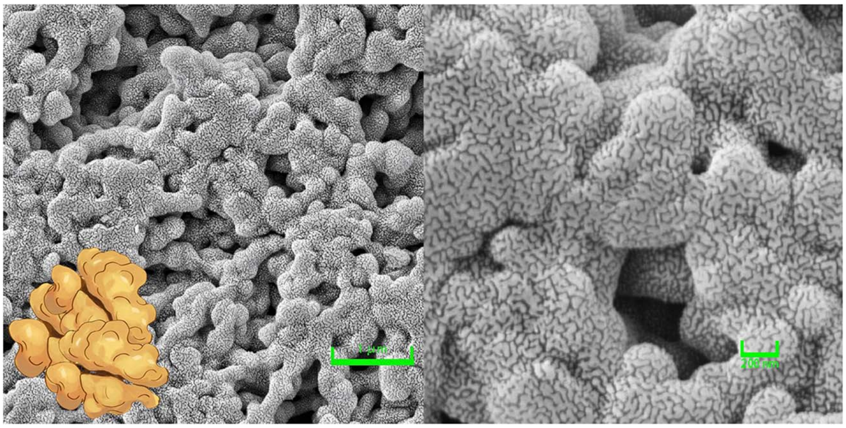

Fig. 4 SEM images of mesoscopic gyrus-like In_2O_3 annealed at 400 °C for 30 min.

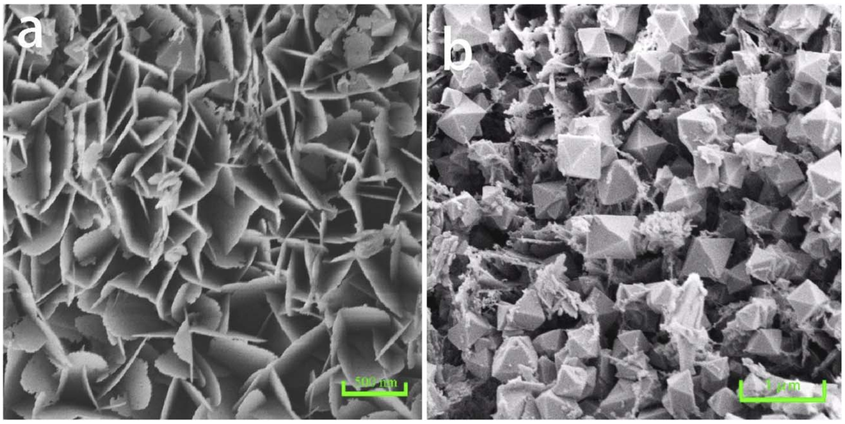

Fig. 5 SEM images of In_2O_3 precursor (without PEO-*b*-PS) annealed at (a) 400 °C for 30 min and (b) 450 °C for 30 min.

stable morphology for In_2O_3 nanocrystals (Fig. 5a and b). Besides, the In_2O_3 particles' inhomogeneity of size was mainly because of the inhomogeneous mass transport between the conversion reactions from nanosheets to lamella layer and octahedral particles (Fig. 5). The XRD patterns of these samples all calcined at 400 °C with different times also confirm the morphological transformation phenomenon (Fig. 3). With the annealing temperature increasing, the diffraction intensity of these samples is gradually increased, indicating that the crystallinity of In_2O_3 is enhanced.

The results above indicate that the copolymer (PEO-*b*-PS) strongly interacts with indium species (In^{3+}) during the assembly process, which reduces the condensation and hydrolysis rates of indium species throughout this synthesis process. Even its presence reduces the indium species' crystallization rate.

3.2. Gas sensing properties of gyrus-like In_2O_3 crystal materials

In_2O_3 has an ordered mesoscopic gyrus-like structure. Because of the low resistivity (high conductivity) of In_2O_3, it has great advantages in high-performance gas sensing (chemical) for its (gyrus structure) high surface area. This not only provides large numbers of O vacancies for the adsorption sites of the sensing gas, but also facilitates the diffusion of guest gas molecules in the surface structure. Besides, due to the charge carriers' fast transport between the surface of gyrus-like structure and the bulk, the prepared In_2O_3 material can provide excellent response/recovery as a chemical gas sensor.

The sensing response of the gyrus-like In_2O_3 sensing film to acetone in the concentration range of 0.5–5 ppm was measured at 150 °C (the content of acetone in diabetic exhaled breath). Based on the definition of $S = R_a/R_g$, the responses for 0.5, 1, 2, and 5 ppm acetone were calculated to be 1.73, 2.67, 3.12 and 3.75, respectively. Limit of detection (LOD) of exhaled breath for the thick-film sensor is below 0.5 ppm for the detection of acetone, which set the threshold for acetone at greater than 0.8 ppm. In addition, the experimental results show that there is a good concentration saturation relationship between the sensing response ($S = R_a/R_g$) and the acetone concentration.

When the gas test box was removed, the exposure of the sensor is from acetone vapor to pure air, the acetone gas molecules immediately being desorbed from the indium trioxide surface and releasing the electrons pre-trapped on the surface. The resistance of the gyrus-like In_2O_3 thick-film sensor can almost return to the original value, indicating that the gas sensor has good reversibility (Fig. 6b). The response–recovery time of the thick-film sensor is also very fast. Taking the gyrus-like In_2O_3 sensor with 1 ppm acetone as an example: the response time is 20 seconds and the recovery time is 16 seconds. Compared to previous reports of acetone sensors based on different In_2O_3 nanostructures, this work's sensors showed better overall sensing performance, such as having a much lower operating temperature (150 °C) which is more amenable

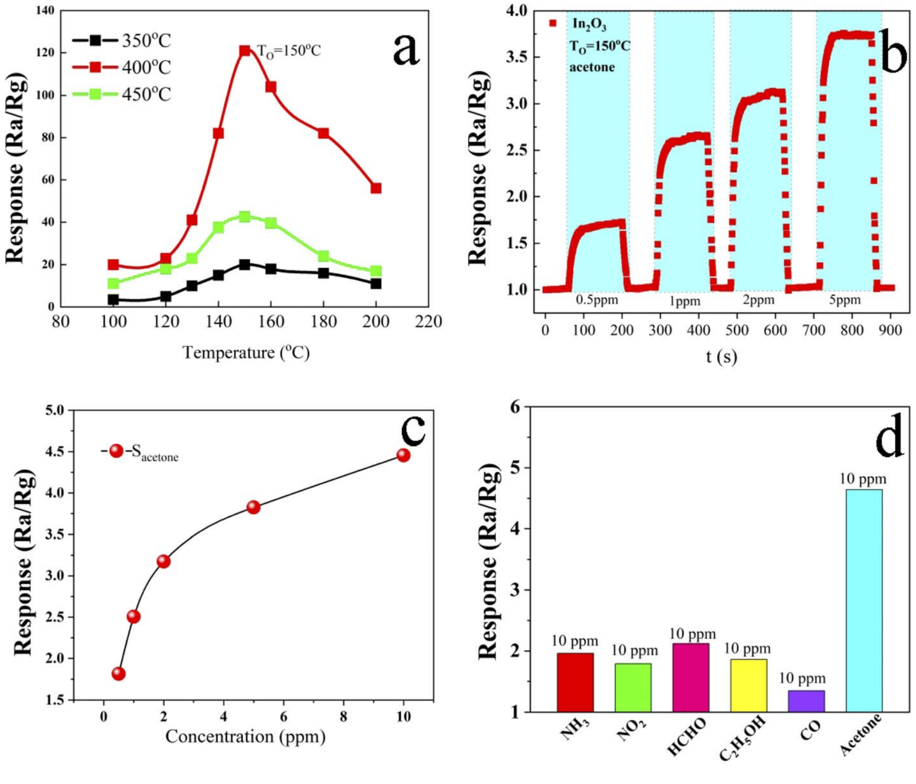

Fig. 6 (a) The response of In_2O_3 nanocrystalline thick-film sensor to 100 ppm acetone at different operating temperatures. (b) The response and recovery curves of the gyrus-like In_2O_3 nanocrystalline sensor to acetone with different concentrations (0.5–5 ppm) at 150 °C. (c) The response (R_a/R_g) of the sensor *vs.* different acetone concentrations. (d) The selectivity of the In_2O_3 sensor to different guest gases (10 ppm) at 150 °C.

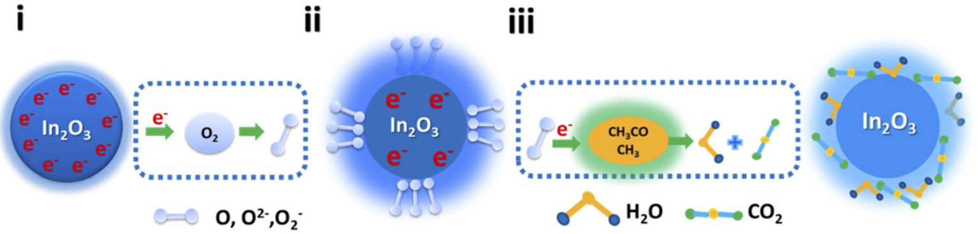

Fig. 7 Schematic illustration of the acetone sensing mechanism of the sensor based on gyrus-like In_2O_3 in air and target gas–air mixture.

for fabricating flexible devices, and also higher sensitivity and much lower LOD, which are because of the following factors. Firstly, the In_2O_3 nanocrystalline material has a uniform nano-gyrus structure (about 40 nm) and the meso-grooved In_2O_3 materials not only facilitate the diffusion of guest gas molecules, but also can provide a large number of activation sites for the adsorption and desorption of acetone gas molecules. Besides, the crystalline particles in the mesoscopic In_2O_3 nanocrystalline structure provide fast transport of charge carriers (electrons) between the sensing film surface and the bulk. So the open mesoscopic gyrus-like structure and high crystallinity lead to excellent low concentration acetone sensing performance.

Gas selectivity is an important parameter of gas sensors, especially in the complex environment of human exhaled breath. In this study, acetone, carbon monoxide, ethanol, ammonia, formaldehyde, and other typical gas molecules were chosen as interference and mixed gases. As shown in Fig. 6d, the response to acetone of the sensor was mainly 5 times higher than that to 5 other selected interfering gases. The phenomenon of the excellent selectivity can be explained as follows: as a typical reducibility gas, the adsorbed oxygen with different valence states on the surface of In_2O_3 is substituted by acetone, which has a stronger ability to capture electrons of n-type In_2O_3 semiconductor than other gases.

The mechanism of a chemoreceptive gas sensor at suitable operating temperature is the conversion (resistance becomes larger and smaller) of electrical resistance between the surface reactions of the gas sensing materials. In_2O_3 is a typical n-type semiconductor. When the sensor was exposed to the air, the oxygen in the air can adsorb on the surface of In_2O_3 to form ionic oxygen species (O^-, O^{2-}) by capturing electrons from the conduction band of In_2O_3. Reducing/oxidizing gases can change the surface carrier concentration by capturing electrons from or releasing electrons to the conduction band of In_2O_3, acting as electron-donating groups. It is obvious that the amount of adsorbed oxygen species plays an indispensable role in the performance of the sensor. As the operating temperature increases, the In_2O_3-based sensors exhibit different sensitivity to acetone vapor at >150 °C, which may be due to the small coverage of adsorbed oxygen as well as a small change in resistivity below the LOD.

Therefore, when the gas sensor is exposed to acetone gas, the resistance of the sensor increases sharply. By contrast, the oxygen species may oxidize the interfering gas molecules, and such oxygen species (O^-, O^{2-}) are expended by the interfering gas molecules, and the electrons captured by oxygen are returned to In_2O_3 during the oxidation process. Consequently, setting the same gas sensor exposed to one kind of interfering gas, a response in the negative direction (decrease in resistance value) can be obtained. Under this sensing mechanism, it is obvious that all the typical interfering gases have a limited effect on the detection of acetone gas by the In_2O_3 nanocrystalline sensor. A possible mechanism of In_2O_3 and the sensing gas reaction process is shown in Fig. 7.

4. Conclusion

In summary, a di-block copolymer-induced method has been developed for the synthesis of gyrus-like indium oxides, which used high-molecular-weight di-block copolymer PEO-*b*-PS as a revulsive, and the indium source is indium chloride. THF/ethanol was used as the solvent. By the support of PS segments during the reaction, ordered gyrus-like In_2O_3 was obtained with a crystalline nanostructure of about 40 nm with high surface area. The obtained gyrus-like In_2O_3 nanocrystalline material was fabricated into thick-film sensors which can work at a relatively low temperature of about 150 °C. Also, the thick-film sensor exhibits an excellent sensing performance with a fast response–recovery time. And the LOD of 0.5 ppm is perfect for use as a diabetic exhaled gas (healthy range is 0.3–0.8 ppm) sensor, and shows very fine selectivity, which may be due to the high porosity of the gyrus-like In_2O_3 and the unique nanocrystalline framework. In conclusion, such excellent performance of the material in this work shows promise for fabricating In_2O_3-based sensors for application in non-invasive diagnosis of diabetes mellitus and preliminary screening. Furthermore, the nanocrystalline gyrus-like In_2O_3 with special structure can be expected to be used in many other applications, such as lithium storage, photocatalysis and so on. It has an important practical significance.

Conflicts of interest

There are no conflicts to declare.

Acknowledgements

This work was supported by Shandong Natural Science Foundation (no. ZR2019BEM036) and Shandong Jianzhu University Doctor's Foundation (X19009Z).

References

1 L. Huo, M. Yang, H. Zhao, S. Gao and Z. Rong, Electrical properties and acetone-sensing characteristics of $LaNi_{1-x}Ti_xO_3$ perovskite system prepared by amorphous citrate decomposition, *Sens. Actuators, B*, 2009, **143**, 111–118.

2 F. Liu, Y. Guan, R. Sun, X. Liang, P. Sun, F. Liu and G. Lu, Mixed potential type acetone sensor using stabilized zirconia and $M_3V_2O_8$ (M: Zn, Co and Ni) sensing electrode, *Sens. Actuators, B*, 2015, **221**, 673–680.

3 S. Singkammo, A. Wisitsoraat, C. Sriprachuabwong, A. Tuantranont, S. Phanichphant and C. Liewhiran, Electrolytically exfoliated graphene-loaded flame-made Ni-doped SnO_2 composite film for acetone sensing, *ACS Appl. Mater. Interfaces*, 2015, **7**, 3077–3092.

4 K. Musa, S. S. Likhodii and S. C. Cunnane, Breath acetone as a measure of systemic ketosis assessed in a rat model of the ketogenic die, *Clin. Chem.*, 2002, **48**, 115–120.

5 C. C. Wang, Y. C. Weng and T. C. Chou, Acetone sensor using lead foil as working electrode, *Sens. Actuators, B*, 2007, **122**, 591–595.

6 G. A. Reichard, J. C. L. Skutches, R. D. Hoeldtke and O. E. Owen, Acetone metabolism in humans during diabetic ketoacidosis, *Diabetes*, 1986, **35**, 668–674.

7 O. E. Owen, V. E. Trapp, C. L. Skutches, M. A. Mozzoli, R. D. Hoeldtke, G. Boden and G. A. Reichard, Acetone metabolism during diabetic ketoacidosis, *Diabetes*, 1982, **31**, 242–248.

8 C. Deng, J. Zhang, X. Yu, W. Zhang and X. Zhang, Determination of acetone in human breath by gas chromatography-mass spectrometry and solid-phase microextraction with on-fiber derivatization, *J. Chromatogr., B*, 2004, **810**, 269–275.

9 S. B. Patil, P. P. Patil and M. A. More, Acetone vapour sensing characteristics of cobalt-doped SnO_2 thin films, *Sens. Actuators, B*, 2007, **125**, 126–130.

10 M. Punginsang, A. Wisitsora-at, A. Tuantranont, S. Phanichphant and C. Liewhiran, Effects of cobalt doping on nitric oxide, acetone and ethanol sensing performances of FSP-made SnO_2 nanoparticles, *Sens. Actuators, B*, 2015, **210**, 589–601.

11 R. K. Mishra, A. Kushwaha and P. P. Sahay, Cr-induced modifications in the structural, photoluminescence and acetone-sensing behaviour of hydrothermally synthesised SnO_2 nanoparticles, *J. Exp. Nanosci.*, 2014, **10**, 1042–1056.

12 W. X. Jin, S. Y. Ma, A. M. Sun, J. Luo, L. Cheng, W. Q. Li, Z. Z. Tie, X. H. Jiang and T. T. Wang, Synthesis of hierarchical SnO_2 nanoflowers and their high gas-sensing properties, *Mater. Lett.*, 2015, **143**, 283–286.

13 S. Wei, M. Zhou and W. Du, Improved acetone sensing properties of ZnO hollow nanofibers by single capillary electrospinning, *Sens. Actuators, B*, 2011, **160**, 753–759.

14 D. An, X. Tong, J. Liu, Q. Wang, Q. Zhou, J. Dong and Y. Li, Template-free hydrothermal synthesis of ZnO micro/nanomaterials and their application in acetone sensing properties, *Superlattices Microstruct.*, 2015, **77**, 1–11.

15 (*a*) C. Peng, J. Guo, W. Yang, C. Shi, M. Liu, Y. Zheng, J. Xu, P. Chen, T. Huang and Y. Yang, Synthesis of three-dimensional flower-like hierarchical ZnO nanostructure and its enhanced acetone gas sensing properties, *J. Alloys Compd.*, 2016, **654**, 371–378; (*b*) M. Nicolaescu, C. Bandas, C. Orha, V. Purcar and C. Lazau, Development of the Zn-ZnO(Nw)@$CuMnO_2$ Heterojunction by Low Temperature Zn Foil Oxidation for Gas Sensor Fabrication, *Coatings*, 2022, **12**, 1630.

16 N. H. Al-Hardan, M. J. Abdullah and A. A. Aziz, Performance of Cr-doped ZnO for acetone sensing, *Appl. Surf. Sci.*, 2013, **270**, 480–485.

17 D. Chen, X. Hou, T. Li, L. Yin, B. Fan, H. Wang, X. Li, H. Xu, H. Lu, R. Zhang and J. Sun, Effects of morphologies on acetone-sensing properties of tungsten trioxide nanocrystals, *Sens. Actuators, B*, 2011, **153**, 373–381.

18 S. B. Upadhyay, R. K. Mishra and P. P. Sahay, Enhanced acetone response in co-precipitated WO3 nanostructures upon indium doping, *Sens. Actuators, B*, 2015, **209**, 368–376.

19 S. Kim, S. Park, S. Park and C. Lee, Acetone sensing of Au and Pd-decorated WO_3 nanorod sensors, *Sens. Actuators, B*, 2015, **209**, 180–185.

20 L. Wang, Z. Lou, T. Fei and T. Zhang, Enhanced acetone sensing performances of hierarchical hollow Au-loaded NiO hybrid structures, *Sens. Actuators, B*, 2012, **161**, 178–183.

21 C. Wang, J. Liu, Q. Yang, P. Sun, Y. Gao, F. Liu, J. Zheng and G. Lu, Ultrasensitive and low detection limit of acetone gas sensor based on W-doped NiO hierarchical nanostructure, *Sens. Actuators, B*, 2015, **220**, 59–67.

22 H. Shan, C. Liu, L. Liu, S. Li, L. Wang, X. Zhang, X. Bo and X. Chi, Highly sensitive acetone sensors based on La-doped-Fe_2O_3 nanotubes, *Sens. Actuators, B*, 2013, **184**, 243–247.

23 C. Su, C. Liu, L. Liu, M. Ni, H. Li, X. Bo, L. Liu and X. Chi, Excellent acetone sensing properties of Sm-doped-Fe_2O_3, *Appl. Surf. Sci.*, 2014, **314**, 931–935.

24 Z. Zhang, Z. Wen, Z. Ye and L. Zhu, Gas sensors based on ultrathin porous Co_3O_4 nanosheets to detect acetone at low temperature, *RSC Adv.*, 2015, **5**, 59976–59982.

25 S. A. Hakim, Y. Liu, G. S. Zakharova and W. Chen, Synthesis of vanadium pentoxide nanoneedles by physical vapour deposition and their highly sensitive behavior towards acetone at room temperature, *RSC Adv.*, 2015, **5**, 23489–23497.

26 M. Epifani, E. Comini, R. Diaz, A. Genc, T. Andreu, P. Siciliano and J. R. Morante, Acetone sensors based on TiO_2 nanocrystals modified with tungsten oxide species, *J. Alloys Compd.*, 2016, **665**, 345–351.

27 B. Bhowmik, Repeatability and stability of room-temperature acetone sensor based on TiO_2 Nanotubes:

influence of stoichiometry variation, *IEEE Trans. Device Mater. Reliab.*, 2014, **14**, 961–967.

28 H. Bian, S. Ma, A. Sun, X. Xu, G. Yang, J. Gao, Z. Zhang and H. Zhu, Characterization and acetone gas sensing properties of electrospun TiO_2 nanorods, *Superlattices Microstruct.*, 2015, **81**, 107–113.

29 C. Wang, J. Zhu, S. Liang, H. Bi, Q. Han, X. Liu and X. Wang, Reduced graphene oxide decorated with CuO–ZnO hetero-junctions: towards high selective gas-sensing property to acetone, *J. Mater. Chem. A*, 2014, **2**, 18635–18643.

30 X. Chi, C. Liu, Y. Li, H. Li, L. Liu, X. Bo, L. Liu and C. Su, Synthesis of pristine In2O3/ZnO–In2O3 composited nanotubes and investigate the enhancement of their acetone sensing properties, *Mater. Sci. Semicond. Process.*, 2014, **27**, 494–499.

31 R. Moos, W. Menesklou, H. J. Schreiner and K. H. Hardtl, Materials for temperature independent resistive oxygen sensors for combustion exhaust gas control, *Sens. Actuators, B*, 2000, **67**, 178–183.

32 G. Hagen, A. Dubbe, F. Rettig, A. Jerger, Th. Birkhofer, C. Plog and R. Moos, Selective impedance based gas sensors for hydrocarbons using ZSM-5 zeolite films with chromium(III) oxide interface, *Sens. Actuators, B*, 2006, **67**, 441–448.

33 F. Rettig, R. Moos and C. Plog, Poisoning of temperature independent resistive oxygen sensors by sulfur dioxide, *J. Electroceram.*, 2004, **13**, 733–738.

34 Z. Zhu, Z. Tao, L. Bi and W. Liu, Investigation of SmBaCuCoO^{5+}double-perovskite as cathode for proton-conducting solid oxide fuel cells, *Mater. Res. Bull.*, 2010, **45**, 1771–1774.

35 J. Wang, F. Meng, T. Xia, Z. Shi, J. Lian, C. Xu, H. Zhao, J. M. Bassat and J. C. Grenier, Superior electrochemical performance and oxygen reduction kinetics of layered perovskite $PrBa_xCo_2O_5$+ ($x = 0.90–1.0$) oxides as cathode materials for intermediate-temperature solid oxide fuel cells, *Int. J. Hydrogen Energy*, 2014, **39**, 18392–18404.

36 J. Zhu, H. Li, L. Zhong, P. Xiao, X. Xu, X. Yang, Z. Zhao and J. Li, Perovskite oxides: preparation, characterizations, and applications in heterogeneous catalysis, *ACS Catal.*, 2014, **4**, 2917–2940.

37 C. Zhou, Y. Zhang, L. Hu, H. Yin and W. G. Wang, Synthesis characterization, and catalytic activity of Mn-doped perovskite oxides for three-way catalysis, *Chem. Eng. Technol.*, 2015, **38**, 291–296.

38 Y. H. Jang, F. Gervais and Y. Lansac, A-site ordering in colossal magnetoresistance manganite La1-xSrxMnO3 molecular dynamics simulations and quantum mechanics calculations, *J. Phys. Chem.*, 2009, **131**, 094503.

39 K. I. Kobayashi, T. Kimura, H. Sawada, K. Terakura and Y. Tokura, Room-temperature magnetoresistance in an oxide material with an ordered double-perovskite structure, *Nature*, 1998, **395**, 677–680.

40 R. J. H. Voorhoeve, D. W. Johnson, J. P. Remeika and P. K. Gallagher, Perovskite oxides: materials science in catalysis, *Science*, 1997, **195**, 827–833.

41 Y. B. Qin, H. X. Yang, L. Wang, H. F. Tian, C. Ma, Y. Li, H. L. Shi and J. Q. Li, Structure, charge ordering and physical properties of $Yb_2Fe_3O_7$, *Eur. Phys. J. B*, 2010, **75**, 231–236.

42 N. Kimizuka, A. Takenaka, Y. Sasada and T. Katsura, New compounds $Yb_2Fe_3O_7$ and $Lu_2Fe_3O_7$, *Solid State Commun.*, 1974, **15**, 1199–1201.

43 J. H. L. Sun, H. Qin, M. Zhao and K. Fan, Influences of Ca doping and oxygen vacancy upon adsorption of CO on the $LaFeO_3$ (010) surface: a first-principles study, *J. Phys. Chem.*, 2011, **115**, 5593–5598.

44 X. Wang, H. Qin, L. Sun and J. Hu, CO_2 sensing properties and mechanism of nanocrystalline LaFeO3 sensor, *Sens. Actuators, B*, 2013, **188**, 965–971.

45 M. Siemons, A. Leifert and U. Simon, Preparation and gas sensing characteristics of nanoparticulate p-type semiconducting $LnFeO_3$ and $LnCrO_3$ materials, *Adv. Funct. Mater.*, 2007, **17**, 2189–2197.

46 P. Song, H. Zhang, D. Han, J. Li, Z. Yang and Q. Wang, Preparation of biomorphic porous LaFeO3 by sorghum straw biotemplate method and its acetone sensing properties, *Sens. Actuators, B*, 2014, **196**, 140–146.

47 Z. L. Wu, R. Zhang, M. Zhao, S. M. Fang, Z. X. Han, J. F. Hu and K. Y. Wang, Effect of Pd doping on the acetone-sensing properties of $NdFeO_3$, *Int. J. Miner., Metall. Mater.*, 2012, **19**, 141–145.

48 T. Chen, Z. Zhou and Y. Wang, Surfactant CATB-assisted generation and gas-sensing characteristics of $LnFeO_3$ (Ln = La, Sm Eu) materials, *Sens. Actuators, B*, 2009, **143**, 124–131.

49 X. Liu, H. Ji, Y. Gu and M. Xu, Preparation and acetone sensitive characteristics of nano-LaFeO3 semiconductor thin films by polymerization complex method, *Mater. Sci. Eng., B*, 2006, **133**, 98–101.

50 J. Hu, X. Liu, B. Cheng, H. Qin and M. Jiang, Acetone gas sensing properties of SmFe1-xMgxO3 perovskite oxides, *Sens. Actuators, B*, 2008, **134**, 483.

51 L. Zhang, H. Qin, P. Song, J. Hu and M. Jiang, Electric properties and acetone-sensing characteristics of $La_{1-x}Pb_xFeO_3$ perovskite system, *Mater. Chem. Phys.*, 2006, **98**, 358–362.

52 M. C. Carotta, M. A. Butturi, G. Martinelli, Y. Sadaoka, P. Nunziante and E. Traversa, Microstructural evolution of nanosized $LaFeO_3$ powders from the thermal decomposition of a cyano-complex for thick film gas sensors, *Sens. Actuators, B*, 1997, **44**, 590–594.

53 S. Huang, H. Qin, P. Song, X. Liu, L. Li, R. Zhang, J. Hu, H. Yan and M. Jiang, The formaldehyde response of $LaFe_{1-x}Zn_xO_3$-based gas sensor, *J. Mater. Sci.*, 2007, **42**, 9973–9977.

54 E. Traversa, S. Matsushima, G. Okada, Y. Sadaoka, Y. Sakai and K. Watanabe, NO_2 sensitive LaFeO3 thin films prepared by r.f. sputtering, *Sens. Actuators, B*, 1995, **25**, 661–664.

55 G. X. Zhu, L. J. Guo, X. P. Shen, Z. Y. Ji, K. M. Chen and H. Zhou, Monodispersed In_2O_3 mesoporous nanospheres: One-step facile synthesis and the improved gas-sensing performance, *Sens. Actuators, B*, 2015, **220**, 977–985.

56 F. L. Gong, Y. Y. Gong, H. Z. Liu, M. L. Zhang, Y. H. Zhang and F. Li, Porous In_2O_3 nanocuboids modified with Pd nanoparticles for chemical sensors, *Sens. Actuators, B*, 2016, **223**, 384–391.

57 A. Shanmugasundaram, B. Ramireddy, P. Basak, S. V. Manorama and S. Srinath, Hierarchical $In(OH)_3$ as a Precursor to Mesoporous In_2O_3 Nanocubes: A Facile Synthesis Route, Mechanism of Self-Assembly, and Enhanced Sensing Response toward Hydrogen, *J. Phys. Chem. C*, 2014, **118**, 6909–6921.

58 L. P. Gao, Z. X. Cheng, Q. Xiang, Y. Zhang and J. Q. Xu, Porous corundum-type In_2O_3 nanosheets: synthesis and NO_2 sensing properties, *Sens. Actuators, B*, 2015, **208**, 436–443.

59 S. M. Wang, B. X. Xiao, T. Y. Yang, P. Wang, C. H. Xiao, Z. F. Li, R. Zhao and M. Z. Zhang, Enhanced HCHO gas sensing properties by Agloaded sunflower-like In_2O_3 hierarchical nanostructures, *J. Mater. Chem. A*, 2014, **2**, 6598–6604.

60 X. M. Xu, D. W. Wang, W. B. Wang, P. Sun, J. Ma, X. S. Liang, Y. F. Sun, Y. G. Ma and G. Y. Lu, Porous hierarchical In_2O_3 nanostructures: hydrothermal preparation and gas sensing properties, *Sens. Actuators, B*, 2012, **171–172**, 1066–1072.

61 L. P. Gao, F. M. Ren, Z. X. Cheng, Y. Zhang, Q. Xiang and J. Q. Xu, Porous corundum-type In_2O_3 nanoflowers: controllable synthesis, enhanced ethanol-sensing properties and response mechanism, *CrystEngComm*, 2015, **17**, 3268–3276.

62 A. Shanmugasundaram, P. Basak, S. V. Manorama, B. Krishna and S. Sanyadanam, Hierarchical Mesoporous In_2O_3 with Enhanced CO Sensing and Photocatalytic Performance: Distinct Morphologies of $In(OH)_3$ via Self Assembly Coupled in Situ Solid–Solid Transformation, *ACS Appl. Mater. Interfaces*, 2015, **7**, 7679–7689.

63 J. J. Liu, G. Chen, Y. G. Yu, Y. L. Wu, M. J. Zhou, H. Q. Zhang, C. D. Lv, H. Qin and X. Qi, Template-free preparation of mesoporous single crystal In_2O_3 achieving superior ethanol gas sensing performance, *RSC Adv.*, 2016, **6**, 14615–14619.

64 Y. H. Li, W. Luo, N. Qin, J. P. Dong, J. Wei, W. Li, S. S. Feng, J. C. Chen, Y. H. Deng and D. Y. Zhao, Highly Ordered Mesoporous Tungsten Oxides with a Large Pore Size and Crystalline Framework for H_2S Sensing, *Angew. Chem., Int. Ed.*, 2014, **53**, 9035–9040.

65 S. Zhang, P. Song, J. Zhang, H. Yan, J. Li, Z. x. Yang and Q. Wang, Highly sensitive detection of acetone using mesoporous In_2O_3 nanospheres decorated with Au nanoparticles, *Sens. Actuators, B*, 2017, **242**, 983–993.

66 S. Park, Acetone gas detection using TiO_2 nanoparticles functionalized In_2O_3 nanowires for diagnosis of diabetes, *J. Alloys Compd.*, 2017, **696**, 655–662.

67 F. Chen, M. Yang, X. Wang, Y. Song, L. Guo, N. Xie, X. Kou, X. Xu, Y. Sun and G. Lu, Template-free synthesis of cubic-rhombohedral-In_2O_3 flower for ppb level acetone detection, *Sens. Actuators, B*, 2019, **290**, 459–466.

68 W. Liu, Y. Xie, T. Chen, Q. Lu, S. Rehman and L. Zhu, Rationally designed mesoporous In_2O_3 nanofibers functionalized Pt catalysts for high-performance acetone gas sensors, *Sens. Actuators, B*, 2019, **298**, 126871.

69 Y. Che, G. Feng, T. Sun, J. Xiao, W. Guo and C. Song, Excellent gas-sensitive properties towards acetone of In_2O_3 nanowires prepared by electrospinning, *Colloid Interface Sci. Commun.*, 2021, **45**, 100508.

70 Z. Song, W. Guan, J. Zeng, B. Zi, D. Xu, W. Wang, Y. Zhang, G. Zhang, Z. Zhu, J. Zhang and Q. Liu, Pt-Sensitized In_2O_3 Nanotubes for Sensitive Acetone Monitoring, *ACS Appl. Nano Mater.*, 2022, **10**, 15611–15618.